Computational Study on the Effect of Particle Shape on Particle-Bubble Interactions Using Discrete Element Method

Youxuan Chen[1], Xin Guo[2], Jianqiang Zhang[3], Junwei Ma[4], Wuxing Du[5] and Yanfang Cui[6]
1. Assistant Engineer
2, 3, 4. Senior Engineer
5, 6. Junior Engineer
Zhengzhou Non-ferrous Metals Research Institute of Chalco (ZRI) and
National Aluminum Smelting Engineering Technology Research Centre,
Zhengzhou, China
Corresponding author: jw_ma@chinalco.com.cn
https://doi.org/10.71659/icsoba2025-bx003

Abstract

Utilizing particle-bubble mechanics theory, we developed a three-dimensional Discrete Element Method (DEM) model to simulate interactions between particles and bubbles. Six distinct irregular particle geometries were incorporated. Simulations examined both spherical and irregularly shaped diaspore particles (0.1 mm, surface-modified) with contact angles of 35.6°, 55.4°, and 85.7° interacting with a stationary bubble in quiescent water. Results indicate a five-stage interaction process for both particle types: free settling, bubble surface flow, liquid film sliding, film rupture and three-phase contact line (TPCL) formation, and TPCL sliding. Compared to spheres, irregular particles exhibited a larger critical collision angle and higher capture probability, alongside a shorter critical induction time. Their edges and vertices facilitate liquid film thinning and rupture between the particle and bubble, thereby reducing induction time and enhancing capture probability.

Keywords: Discrete Element Method, Particle-bubble interaction, Particle shape, Critical collision angle, Critical induction time.

1. Introduction

Flotation is an efficient method for separating fine minerals, which is to achieve selective separation of useful minerals and gangue minerals according to the differences in the physical and chemical properties of the surface of mineral particles [1, 2]. As the basic action unit of the flotation process, the particle-bubble interaction determines the flotation efficiency to a certain extent, which can be divided into three sub-processes: the particle-bubble collision, the particle-bubble attachment, and the particle-bubble detachment. Particle shape characteristics play a crucial role in these sub-processes [3]. Particle shape remarkably affects the induction time and flotation recovery. Induction time is the time interval between the initial contact of the particle and bubble and the formation of a stable three-phase contact line. Verrelli et al. [4, 5] studied the variation of the induction time between spherical and irregular particles at different approach speeds, and the results showed that the induction time between irregular particles and a bubble was an order of magnitude lower than that of spherical particles, and the induction time decreased with the increase of approach speed. Hassas et al. [6] found that irregular surface bulges and sharp edges can effectively trigger the rupture of liquid film and improve the flotation recovery. Wen and Xia [7] found that the low-ash anthracite particles with lower roundness can be floated quickly, while the low-ash anthracite particles with higher roundness floated slowly. Ulusoy [8, 9] states that the study found that particles with higher elongation and less roundness had higher flotation recovery than particles with lower elongation and higher roundness. It is generally believed that the protrusions and sharp edge structures on the surface of irregular particles contribute to the rapid thinning and rupture of the particle-bubble liquid film [10]. Therefore,

irregularly shaped mineral particles usually have higher flotation recovery and flotation rate compared with spherical particles.

However, the effect of particle shape on particle-bubble interactions is difficult to evaluate for the following reasons. First, the particle size of flotation particles is small. It is difficult to describe the three-dimensional shape of the particles, and there is no accepted method to characterize the three-dimensional shape of the flotation particles accurately [11]. Secondly, when preparing particles of various shapes, the surface roughness of the particles also changes [12]. For the above two reasons, it is a great challenge to experimentally study the effect of particle shape on the behavior of particle-bubble interactions.

In recent years, the Discrete Element Method (DEM) was successfully used in simulation to study the particle-bubble interaction problem in flotation. Maxwell et al. [13] developed a DEM model of particle-bubble interaction. They computationally analyzed the effect of particle size distribution and hydrophobic force on particle-bubble collision and particle sliding on the bubble's surface. Moreno-Atanasio [14] compared and studied the effects of different Hydrophobic force models (power decay law and single exponential law) on bubble capturing particles. Gao et al. [15] studied the effect of hydrophobic forces on particle-bubble interactions using a single exponential decay type formula for hydrophobic forces. It is found that when the decay length λ is less than 10 nm, the number of particles captured by the bubbles is independent of the strength of the hydrophobic force, and when λ is in the range of 10-500 nm, the capturing efficiency increases significantly with the strength of the hydrophobic force and λ. In subsequent work, Gao et al. [16] performed DEM modeling based on the Schulze particle-bubble aggregate theory [17] to simulate the sliding of particles on the surface of the bubble and the formation of a TPCL. However, none of these works based on DEM to simulate particle-bubble interactions have considered the effect of particle shape on particle-bubble interactions.

This work presents a 3D computational model of particle-bubble interactions based on the Discrete Element Method (DEM) in quiescent liquid and designs six models of irregularly shaped particles. Spherical particles were used as a control group, and the effects of particle shape on the behavior of particle-bubble interactions, critical collision angle, and capture probability were investigated. Furthermore, the single irregular particle bubble interaction behavior was compared with the reported experimental data to verify the accuracy of the simulation.

2. Simulation Methodology

2.1 Model Description

The three-dimensional schematic diagram of the simulation system is shown in Figure 1. The bubble was fixed at the coordinate origin O in a quiescent water environment. The particles are generated and released in turn along the positive direction of the X-axis on the horizontal plane $3R_b$ (R_b = bubble radius) above the bubble center O. In other words, each particle generation position is a certain distance more in the positive direction of the X-axis than the last particle generation position. The positions where the particle is generated are cycled in this way until the particle is released at a specific position on the X-axis, and the bubble cannot capture the particle. In this simulation, the position where the particle velocity reaches the minimum value during the process of a particle approaching the bubble was set as the collision point. The angle between the line connecting the center of the bubble and the collision point and the positive direction of the Z-axis was defined as the collision angle (φ).

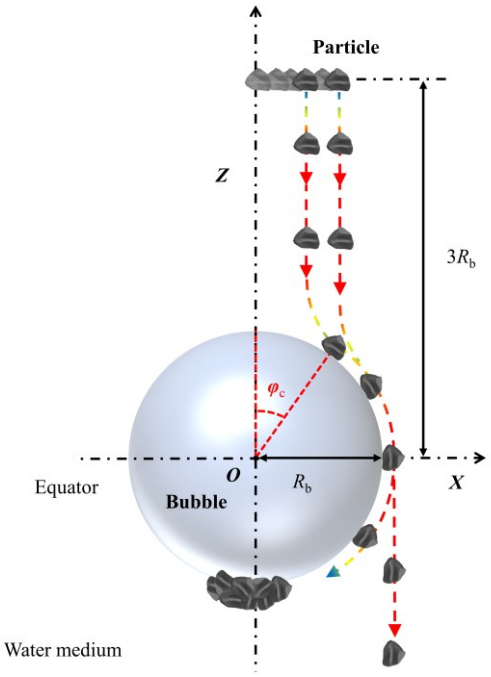

Figure 1. Schematic diagram of simulation system.

2.2 Discrete Element Method (DEM)

The Discrete Element Method (DEM), invented by Cundall and Strack [18], has become an effective tool for studying the dynamic behavior of particle systems. The basic concept is to discretize the research object into individual rigid elements governed by Newton's second law.
A computer code has been developed in Particle Flow Code (PFC) to simulate the interaction behavior between particle and bubble. The code will calculate and update the surface distance between the particle and the bubble at each time step, thereby calculating the particle-bubble interaction force. Finally, the acceleration of the particles is calculated by Newton's second law, and the velocity and displacement of the particles are obtained by integration.

2.3 Particle-bubble Mechanical Model

In fact, during particle-bubble interactions, most of the forces acting on the particles depend on the shape of the particles, such as resistance, capillary forces, etc. Because the mechanical model of irregular particles is relatively complex, the mechanical model of irregular particles is simplified in this work, and the mechanical model of irregular particles and bubbles is equal to the mechanical model of spherical particles and bubbles. A schematic of particle-bubble interaction is shown in Figure 2. During particle-bubble interactions, the following forces act on the particles, namely: (1) gravity force, (2) buoyancy force, (3) hydrodynamic drag force (lubrication and stokes drag force), (4) surface forces (electrostatic force, van der Waals force, hydrophobic force), (5) capillary force, (6) pressure force (hydrostatic and Laplace pressure), and (7) contact force. A brief description of each of these forces is presented below.

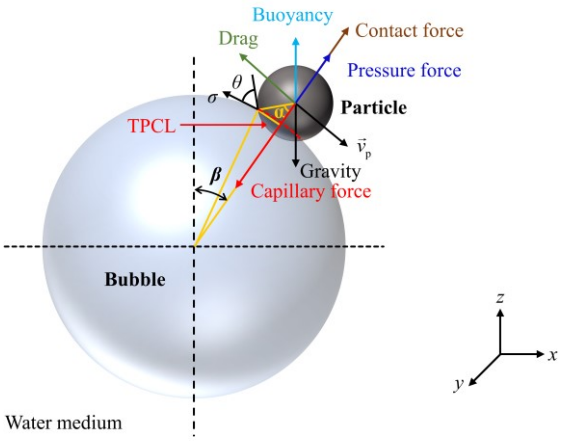

Figure 2. Schematic of particle-bubble interaction (β = polar angle, α = central angle, θ = contact angle, σ = surface tension, TPCL = three phase contact line (red dotted line), $\vec{v}_p$ = particle velocity).

2.3.1 Gravity Force

The gravitational force $\boldsymbol{F_G}$ acting on a spherical particle of radius R_p and density ρ_p can be expressed as:

$$\boldsymbol{F_G} = \frac{4}{3} {R_p}^3 \rho_p \, \boldsymbol{g} \tag{1}$$

where $\boldsymbol{g}$ is the gravitational acceleration constant given as 9.8 m/s^2, in the negative Z-axis direction.

2.3.2 Buoyancy Force

The buoyancy of a particle of radius R_p in a liquid with density ρ_l can be expressed as:

$$\boldsymbol{F_B} = -\frac{1}{3}\pi \, {R_p}^3 \rho_l (2 + 3\cos\alpha - \cos^3\alpha) \, \boldsymbol{g} \tag{2}$$

where α is the central angle, which is the filling angle measured from the bubble–particle centreline to the connecting line of the particle center to the three-phase contact. When there is no physical contact between particles and bubbles, α is equal to zero.

2.3.3 Hydrodynamic Drag Force

Under the particle, the Reynolds number is always smaller than 1, the drag force on the particle can be calculated by Stokes' law as:

$$\boldsymbol{F_{drag}} = -6\pi \, \mu \, R_p \, \rho_p \, \boldsymbol{v_p} \tag{3}$$

Where μ is the viscosity of the fluid and $\boldsymbol{v_p}$ is the velocity of the particle.

However, when the particle approaches the bubble of radius R_b, the intervening liquid layer exerts a force (lubrication resistance) on the particles opposing their movements. Macroscopically, when

the particle approaches the bubble surface, the particle will make a flow around the bubble surface, and the motion trajectory will change. As a result of the gap between particle and bubble surface being particle diameter range, the Taylor equation is almost consistent with the reported experimental data [19]. The Taylor equation given by Nguyen and Schulze is as follows [20]:

$$\boldsymbol{F_{res}} = -6\pi\,\mu\,\frac{1}{h}\,\frac{R_p+R_b}{R_pR_b}\,\boldsymbol{v_r} \tag{4}$$

where $\boldsymbol{v_r}$ is the radial velocity of approach of the particle to the bubble and h is the surface distance between particle and bubble.

2.3.4 Surface Forces

The extended DLVO (Derjaguin-Landau-Verwey-Overbeek) theory, namely EDLVO theory [21], holds that there are three forces in the interaction between particle and bubble in the flotation system, namely, van der Waals force, electrostatic force, and hydrophobic force. Assuming spheres with radius R_p and R_b of the particle and the bubble, respectively, then the van der Waals force between the particle and the bubble can be expressed as:

$$\boldsymbol{F_v} = -\frac{A_{132}}{6h^2}\frac{R_pR_b}{R_p+R_b}\,\boldsymbol{n} \tag{5}$$

where A_{132} is the Hamaker constant of particle and bubble in the medium (water), $\boldsymbol{n}$ is the unit vector directed towards the particle from the bubble along the particle-bubble centerline.

$$A_{132} = (\sqrt{A_{11}} - \sqrt{A_{33}})(\sqrt{A_{22}} - \sqrt{A_{33}}) \tag{6}$$

where A_{11}, A_{22}, and A_{33} are the respective Hamaker constants for particle, bubble, and medium (water) in vacuum, J.

The electrostatic forces $\boldsymbol{F_E}$ between particle and bubble can be expressed as:

$$\boldsymbol{F_E} = \pi\,\varepsilon_0\varepsilon\,\frac{R_pR_b}{R_p+R_b}\,(\psi_{01}{}^2 + \psi_{02}{}^2)\left[\frac{2\,\psi_{01}\,\psi_{02}}{\psi_{01}{}^2+\psi_{02}{}^2}p' + q'\right]\boldsymbol{n} \tag{7}$$

$$p' = -\frac{2\kappa\exp(-\kappa h)}{\left[1+\exp(-\kappa h)\right]\left[1-\exp(-\kappa h)\right]} \tag{8}$$

$$q' = \frac{2\kappa\exp(-2\kappa h)}{1-\exp(-2\kappa h)} \tag{9}$$

where :

ψ_{01} surface potential of particle, mV

ψ_{02} surface potential of bubble, mV

(which can be replaced by the Zeta potential)

ε_0 permittivity of water in a vacuum, 8.851×10^{-12} C^2/J·m

ε relative permittivity of water, 78.5

κ inverse of the 96 nm Debye length [22].

The calculation of hydrophobic force $\boldsymbol{F_H}$ can usually be quantitatively described by two formulas, namely, an exponential decay law (single exponential and double exponential) and a power decay law [23]. Since there is no generally accepted formula for calculating hydrophobic force, the formula of hydrophobic force was chosen for this simulation as the power decay law. The power decay law given by Yoon is as follows [24]:

$$\boldsymbol{F_H} = -\frac{K_{132}}{6h^2}\frac{R_p R_b}{R_p + R_b}\,\boldsymbol{n} \tag{10}$$

$$K_{132} = \sqrt{K_{131}K_{232}} \tag{11}$$

where K_{131}, K_{232}, and K_{132} are the hydrophobic force constants of particle and particle, bubble and bubble, particle and bubble in the medium (water).

It is noteworthy that Equations 5, 7 and 10 tend to infinity when the distance between the particle and bubble approaches zero. Therefore, a cut-off value of 0.5 nm was considered in the simulations to prevent computational errors [13]. This cut-off provides a maximum value of van der Waals, electrostatic, and hydrophobic forces acting on the particles.

2.3.5 Capillary Force

Capillary force $\boldsymbol{F_{cap}}$ is the primary attachment force between particle and bubble. The capillary force acting along the TPCL plays a vital role in maintaining the particle attachment to the bubble [25]. Capillary force can be expressed as:

$$\boldsymbol{F_{cap}} = -2\pi\, R_p\, \sigma\, \sin\alpha\, \sin(\theta - \alpha)\, \boldsymbol{n} \tag{12}$$

where:
σ surface tension, N/m
θ contact angle
α central angle.

2.3.6 Pressure Force

The pressure force $\boldsymbol{F_P}$ is defined as the difference between the Laplace pressure and the hydrostatic pressure, it can be expressed as:

$$\boldsymbol{F_P} = \pi\, {R_p}^2\, \sigma\, \sin^2\alpha \left[\frac{2\sigma}{R_b} - \rho_1\, g\, H\right]\, \boldsymbol{n} \tag{13}$$

where H is the height difference between the bubble vertex and the center of the TPCL.

2.3.7 Contact Force

Many research reported that when particles collide with bubbles, like elastic contact, the particles slightly bounce off the bubble's surface [26]. This contact force $\boldsymbol{F_{cont}}$ is calculated using a linear contact model based on linear springs and dashpot [27]. Considering the overlap of particle and bubble during the collision, the normal component of contact force was calculated as follows [15, 26, 28]:

$$\boldsymbol{F_{cont}} = k\,\delta\,\boldsymbol{n} - \eta\,\boldsymbol{v_r} \tag{14}$$

$$\eta = 2\sqrt{\frac{m_p m_b k}{m_p + m_b}}\ \frac{\ln e}{\sqrt{\pi^2 + (\ln e)^2}} \tag{15}$$

Where:
k spring stiffness, N/m
δ overlapped distance
μ damping coefficient
m_p mass of the particle
m_b mass of the bubble
e coefficient of restitution.

Finally, each of the above forces is added to the linear contact model built into the PFC software as an additional force. In this contact model, the motion of particles includes translation and rotation.

2.4 Simulation Parameters and Initial Conditions

The spherical particle with a diameter of 0.1 mm and a density of 3.3 g/cm³ as well as six irregular shape particles (equal volume spherical equivalent diameter is 0.1 mm) were selected for this simulation. Particle properties are the same as diaspore particles (surface-modified), with contact angles of 35.6°, 55.4°, and 85.7°. The diameter of the bubble was 1 mm, and the surface potential of the bubble was -45 mV. The simulation parameters are listed in Table 1. The particle properties are listed in Table 2. The value of the hydrophobic force constant K_{132} is derived from the experimental data of Yoon [22]. The particle shape parameters are listed in Table 3. The three-dimensional model of irregular shape particles is shown in Figure 3.

Table 1. Simulation parameters.

Parameters	**Value**
Water density ρ_l (kg/m^3)	1000
Water viscosity μ (Pa·s)	0.001
Surface tension of gas-water σ (N/m)	0.072
Restitution coefficient of bubble-particle contact	0.2
Stiffness of particle-bubble contact k (N/m)	1
Time step Δt (s)	1×10^{-7}

Table 2. Particle property parameters.

Parameters	Value		
Contact angle θ (°)	35.6	55.4	85.7
Surface potential ψ (mV)	-28.6	-25.2	-28.6
Hamaker constant A_{132} (J)	9.32×10^{-22}	8.75×10^{-21}	9.32×10^{-22}
Hydrophobic force constant K_{132} (J) [22]	0	2.62×10^{-19}	0

Table 3. Particle shape parameters.

Shape	Irregular-a	Irregular-b	Irregular-c	Irregular-d	Irregular-e	Irregular-f
Volume (mm^3)	0.00419	0.00419	0.00419	0.00419	0.00419	0.00419

Surface area (mm^2)	0.147	0.151	0.152	0.157	0.158	0.168
Sphericity	0.856	0.833	0.826	0.799	0.798	0.746

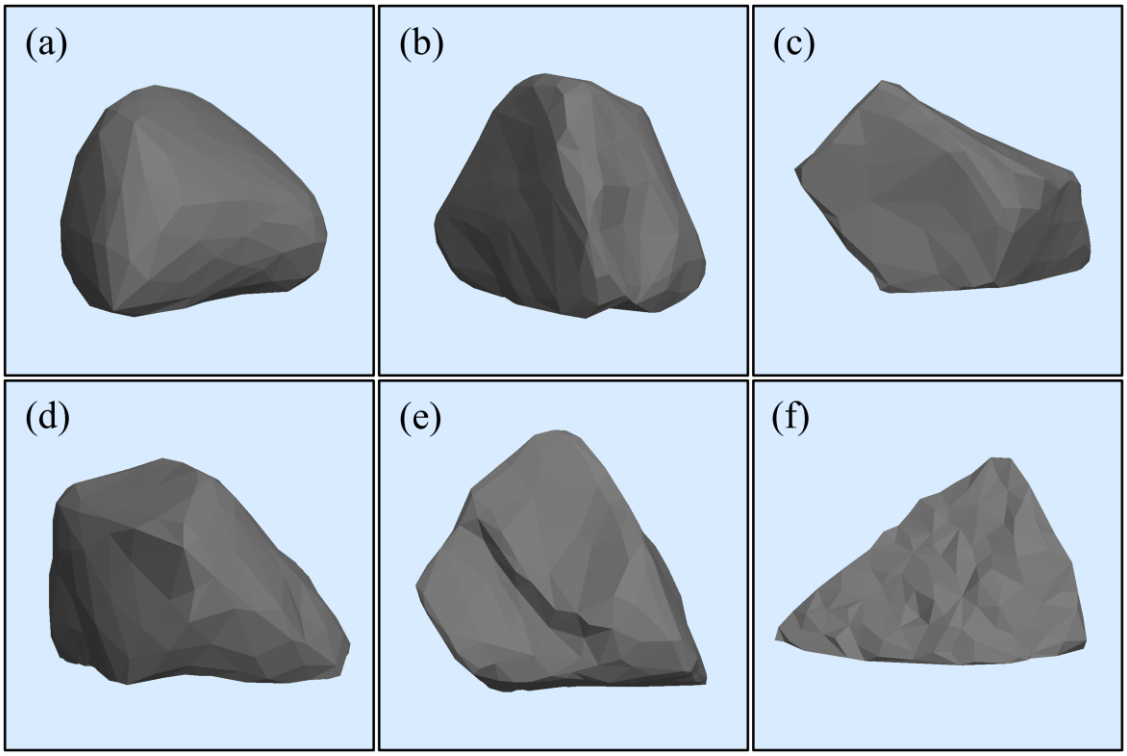

Figure 3. Schematic diagram of the three-dimensional model of irregular particles.

3. Results and discussion

3.1 Effect of particle shape on the interaction behavior of particle-bubble

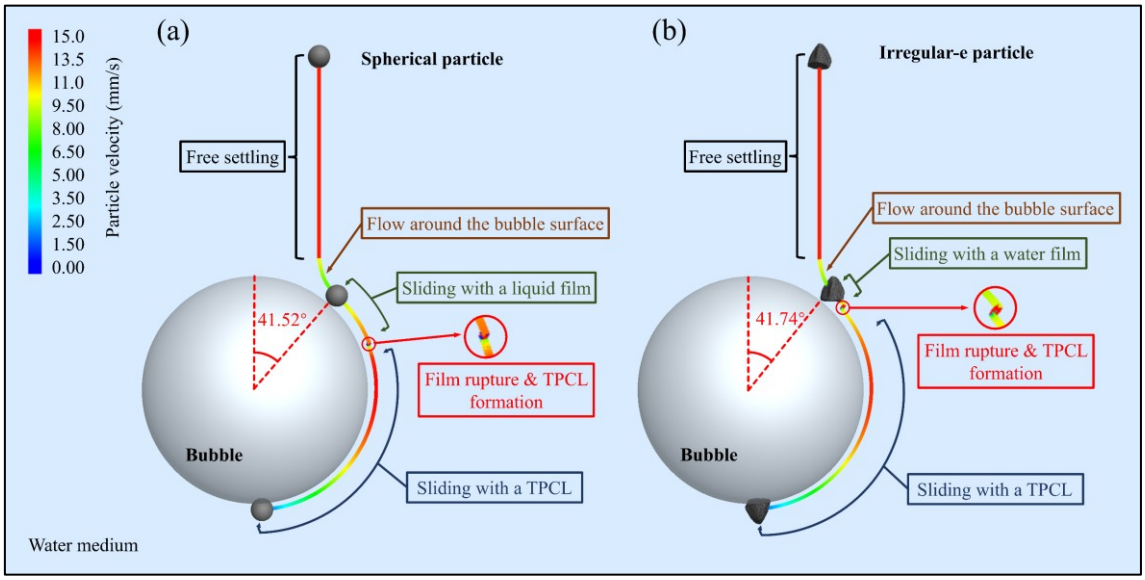

Figure 4. Comparison particle-bubble interaction behaviour (a) spherical particle (b) irregular-e particle.

Irregular-e particle is a typical irregular shape particle. The following will take the irregular-e particle as an example to analyze the effect of particle shape on the interaction behavior between particle and bubble. Figure 4 shows the simulation results of the interaction between spherical particle (contact angles of 55.4°, collision angle 41.52°) and irregular-e particle (contact angles of 55.4°, collision angle 41.74°) and bubble. From the simulation results, the interaction behavior of spherical particles and irregular-e particles with the bubble can be divided into five stages: (1) Stage of free settling: the particle reaches the terminal velocity after a short acceleration and then begins to move at a uniform velocity. (2) Stage of flow around the bubble surface: when the particle gradually approaches the bubble surface, because the water molecules between the particle and bubble are continuously discharged, the lubrication resistance (direction from the bubble to the particle) is acted on the particle, resulting in the particle moving around the bubble surface, and the motion trajectory is changed. (3) Stage of sliding with a liquid film: after the collision between particle and bubble, the particle slides on the liquid film between particle and bubble. (4) Stage of Film rupture & TPCL formation: when the particle-bubble liquid film thickness is thinned to the critical liquid film thickness, the particle will rupture the liquid film to form a TPCL and expand to a stable state. (5) Stage of sliding with a TPCL: after the TPCL is formed between particle and bubble, the particle continues to slide down the bubble surface and finally stays at the bottom of the bubble under the combined action of capillary force, pressure, buoyancy, and gravity.

However, although the five stages mentioned above all exist in the interaction behavior of the six irregular shape particles and bubbles, due to the significant differences in the shapes of the six irregular shape particles, the duration of each stage will be different.

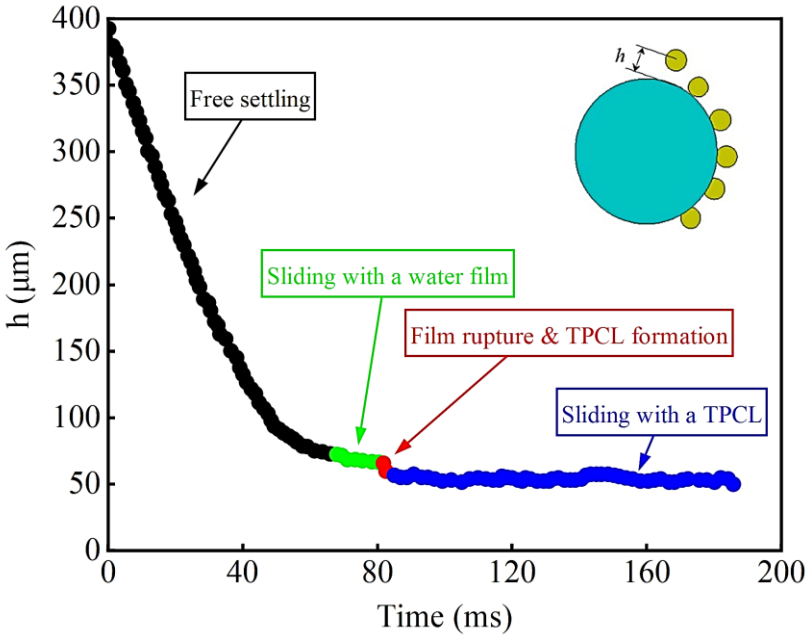

Figure 5. Particle-bubble spacing distance as a function of time.

The simulation results of the interaction behavior between particle and bubble are consistent with each stage of the interaction behavior between glass bead and bubble observed by Nguyen and Evans [29] using the Milli-timer device. The experimental results are shown in Figure 5.

As shown in Figure 6, the simulated interaction behavior of irregular-f particle and bubble is relatively consistent with the interaction behavior of particle and bubble observed by Zhuo et al. [30] experiment.

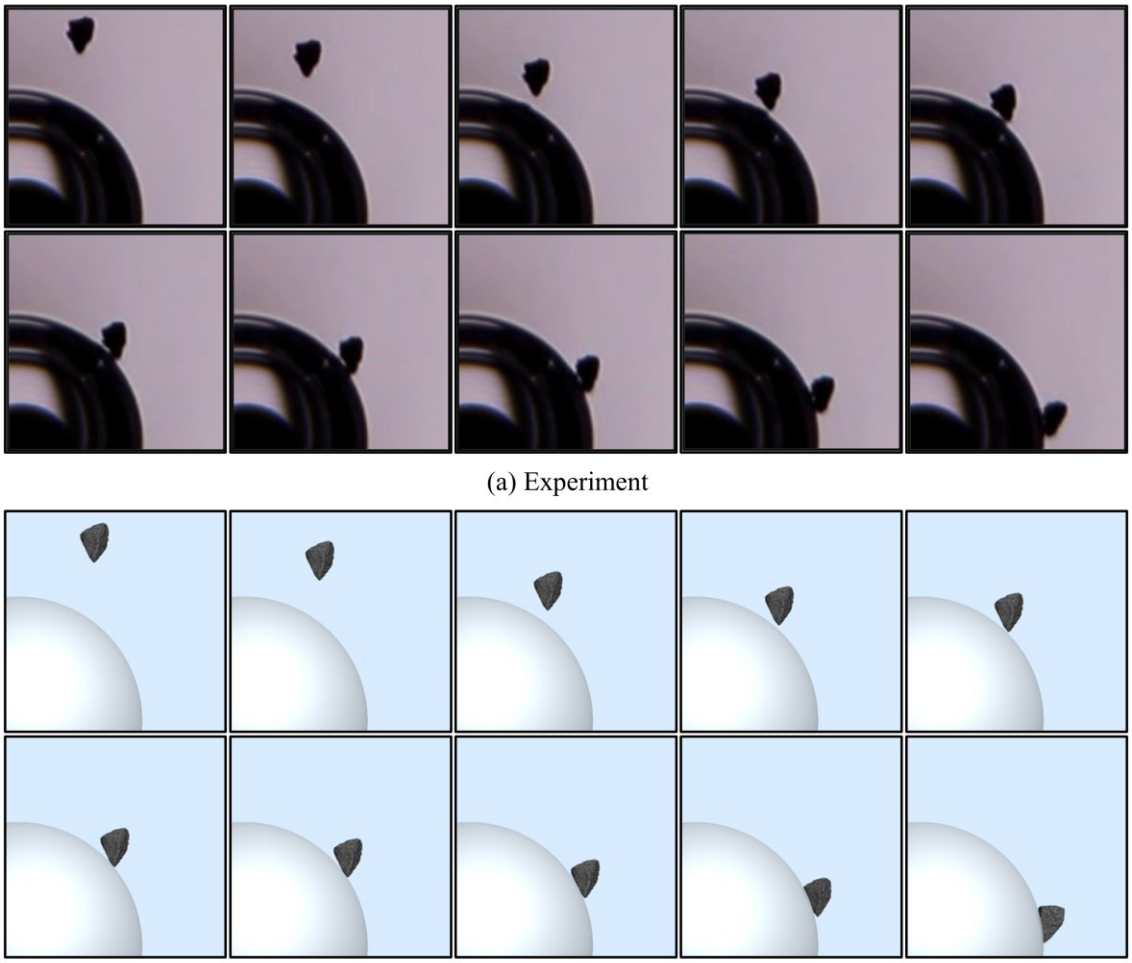

(a) Experiment

(b) Simulation

Figure 6. Comparison particle-bubble interaction behaviour (a) experiment and (b) simulation (irregular-f particle).

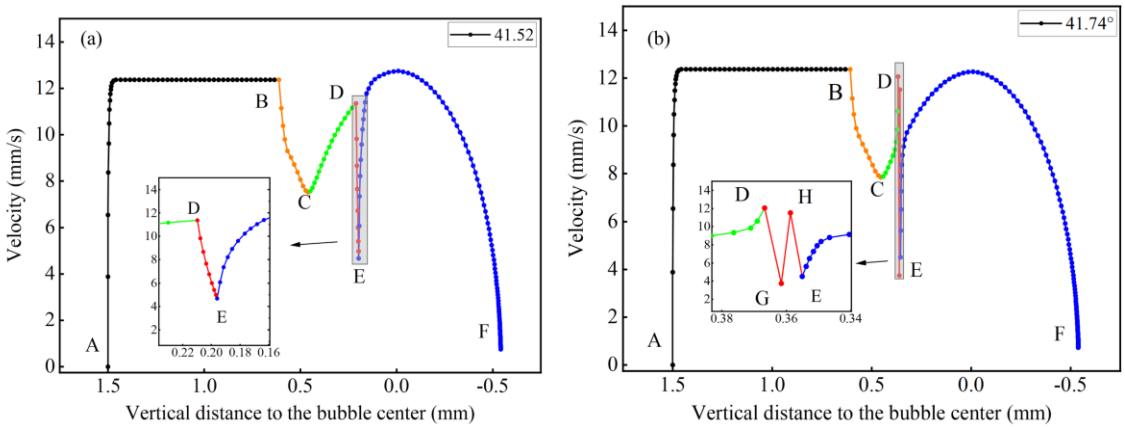

Figure 7. Diagram of particle velocity (a) spherical particle and (b) irregular-e particle.

Figure 7 (a) and (b) show the velocity variation curves of the spherical particle (contact angles of 55.4°, collision angle 41.52°) and irregular-e particle (contact angles of 55.4°, collision angle 41.74°) The velocity curves of spherical and irregular-e particles can also be divided into five stages: (1) Segment A-B is the stage of free settling: after a brief acceleration, the particle reached terminal velocity (12.42 mm/s) and then approached the bubble at this velocity. (2) Segment B-C is the stage of flow around the bubble surface: before the particle collides with the bubble, the particle will flow around the upper hemisphere of the bubble. The velocity of spherical particles decreased from 12.42 to 7.51 mm/s, which decreased by 39.51 %. The velocity of an irregular-e particle is reduced from 12.42 to 7.87 mm/s, which is reduced by 36.63 %. Point C is the collision point between particle and bubble. (3) Segment C-D is the stage of sliding with a liquid film: after the particle collides with a bubble, the particle immediately slides along the liquid film on the bubble surface. In this stage, the sliding velocity of spherical and irregular-e particles increases from 7.51 to 11.40 mm/s and from 7.87 mm/s to 12.93 mm/s, respectively. (4) Segment D-E is the stage of film rupture & TPCL formation. When the liquid film thickness between particle and bubble decreases to the critical liquid film thickness, the particle ruptures the liquid film to form a TPCL, and the TPCL expands to a stable state. In this process, the particle velocity will decrease sharply. The sliding speed of spherical particles decreased from 11.40 to 4.70 mm/s. The sliding speed of irregular-e particle first decreased from 12.11 to 3.73 mm/s, then increased to 11.55 mm/s, and finally reduced to 4.50 mm/s. (5) Segment E-F is the stage of sliding with a TPCL: particle continues to slide along the bubble surface based on the TPCL, and the sliding speed gradually increases. When the particle reached near the "equator" position of the bubble, the particle sliding speed reached a maximum (The maximum velocities of spherical and irregular-e particles are 12.72 and 12.32 mm/s, respectively). After the particle crossed the bubble "equator" position, the sliding speed of the particles gradually decreased and finally stayed at the bubble bottom.

However, comparing and analyzing Figure 7 (a) and (b), the velocity variation difference between spherical and irregular-e particles is mainly in C-E Segment. The time elapsed by the C-E segment is also defined as the induction time, which is the time elapsed from the instant of collision to the establishment of a stable TPCL [4, 31]. The duration of the C-E Segment of the spherical particle is 136 ms, and that of the irregular-e particle is 78 ms. The analysis shows that irregular particles have angular and edge shapes compared with spherical particles, making it easier to rupture the water film between particles and bubbles, thereby significantly reducing the thinning and rupture time of the liquid film. In segment D-E, the velocity variation of the irregular-e particle has a more considerable fluctuation than that of the spherical particle. When the irregular-e particle ruptures the liquid film, the edges and corners of the particle and the bubble first form a TPCL, which causes the irregular-e particle to lose balance and rotate. (see Figure 8). Point D in Figure 7 (b) corresponds to Figure 8 (a), Segment G-H corresponds to Figure 8 (b)-(g), Point E corresponds to Figure 8 (h).

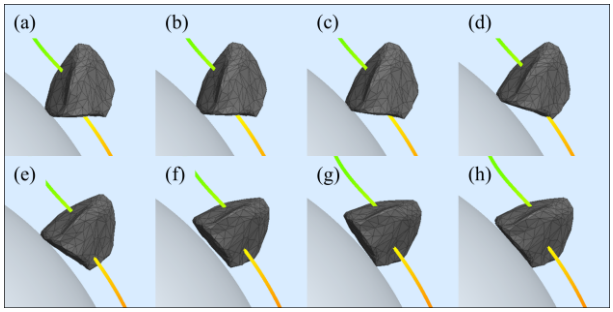

Figure 8. Schematic diagram of irregular particle rotation (colour online).

The simulation results of particle velocity are consistent with the velocity variation particles measured by Zhuo et al. [32] experiment (particle size 0.15-0.1 mm, density 3.4 g/cm^3, collision

angle 50.91°). The experimental results are shown in Figure 9. The main difference between this simulation and its experiment is in Segment D-E in Figure 7 (a) and (b). The experimental results do not reflect the process of liquid film rupture and TPCL formation between particle and bubble. The small space-time scale of the D-E process leads to the failure of its multi-target tracking software to capture this process.

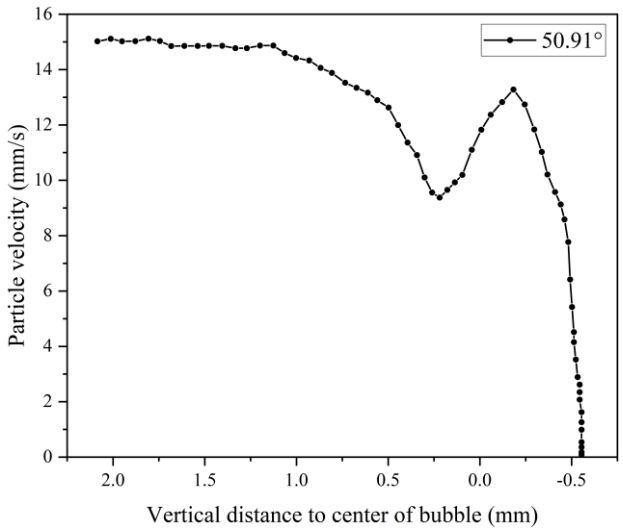

Figure 9. Diagram of particle velocity.

3.2 Effect of Particle Shape on Critical Collision Angle

In this simulation, the critical collision angle (φ_c) was defined as: when the collision angle (φ) between particle and bubble is less than or equal to the critical collision angle (φ_c), the particle will be captured by the bubble, otherwise, the particle will not be captured by bubble. As shown in Figure 10, take an irregular-e particle (contact angles of 55.4°, critical collision angle 45.30°) as an example. A particle would be captured by a bubble when $\varphi_1 < \varphi_c$, while the particle will not be captured by a bubble when $\varphi_2 > \varphi_c$.

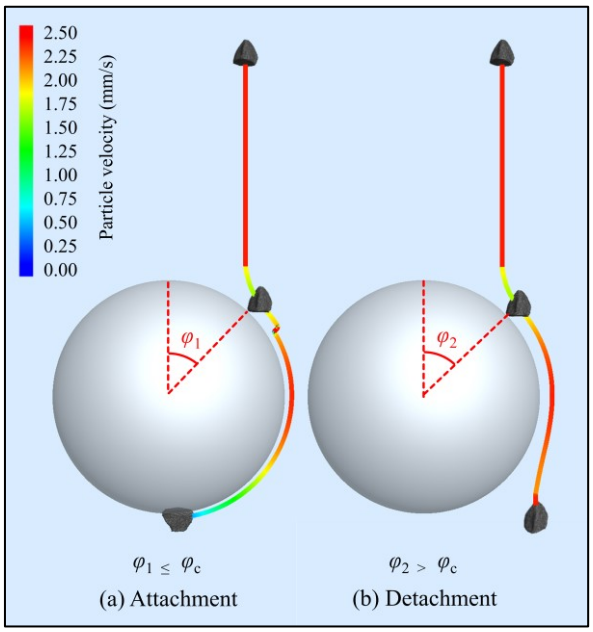

Figure 10. Schematic diagram of critical collision angle.

To investigate the effect of particle shape on the critical collision angle, the critical collision angles of spherical particles and irregular (a-f) particles with contact angles of 35.6°, 55.4° and 85.7° were simulated. The simulation process found that the critical collision angle of irregular particles is related to the particle settlement posture. The critical collision angle between different settlement postures is significantly different. Therefore, when simulating the critical collision angle of irregular (a-f) particles, each irregular-shaped particle needs to obtain the critical collision angle under 12 settlement postures and take its average value to avoid the influence of particle settlement posture on the critical collision angle.

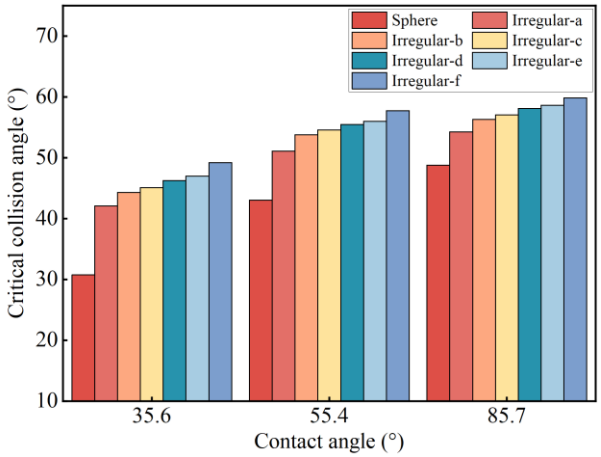

Figure 11. Critical collision angle and particle shape.

Figure 11 illustrates the effect of particle shape on the critical collision angle between particle and bubble. As we can see, at the same contact angle, the critical collision angle of the spherical particle is the smallest, and the irregular (a-f) particles increase sequentially. The critical collision angle between spherical and irregular (a-f) particles and bubbles decreases with increasing contact angle. For example, the particle contact angle increased from 35.6° to 85.7°, and the critical collision angle of spherical and irregular shape (a-f) particle and bubble decreased by 18.02°, 12.12°, 11.97°, 11.92°, 11.85°, 11.66°, and 10.65°. The arithmetic means of the critical collision angle of irregular (a-f) particles is 8.59°, 11.72°, and 18.46° higher than that of spherical particles with the same contact angle when the particle contact angle is 35.6°, 55.4°, and 85.7°. In other words, the effect of particle shape on the critical collision angle is enhanced with the weakening of particle hydrophobicity. At the same contact angle, the critical collision angle of irregular shape particles increases with the decrease of sphericity of irregular shape particles. For example, at a contact angle of 55.4° the sphericity of the irregular (a-f) particles decreased from 0.856 to 0.746, while their critical collision angle increased from 51.12° to 57.73°. It shows that the more the shape of irregular shape particles is away from the sphere, the greater the critical collision angle between irregular shape particles and bubbles. All of these prove that irregular shape particles have larger critical collision angles than spherical particles.

3.3 Effect of Particle Shape on Capture Probability

When the collision angle between the particle and the bubble is the critical collision angle, the horizontal distance between the release position of the particle and the *Z*-axis is the critical collision radius R_c. The schematic diagram of the critical collision radius is shown in Figure 12. Since the detachment of particles after attachment to a bubble is not considered in this simulation, the particle will not fall if the bubble captures them. Therefore, the capture probability of particles can be calculated according to the formula of capture probability [22] and collision probability [33].

$$P_{cap} = P_c\, P_a\, (1 - P_d) \tag{16}$$

$$P_c = \left(\frac{R_c}{R_b}\right)^2 \tag{17}$$

where :

P_{cap} capture probability
P_c collision probability
P_a attachment probability
P_d detachment probability
R_c collision radius

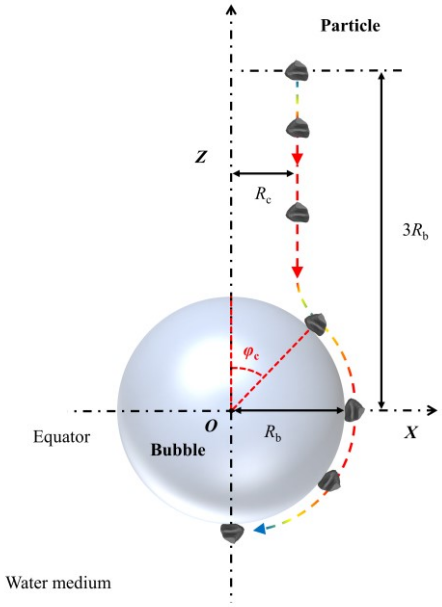

Figure 12 Schematic diagram of critical collision radius.

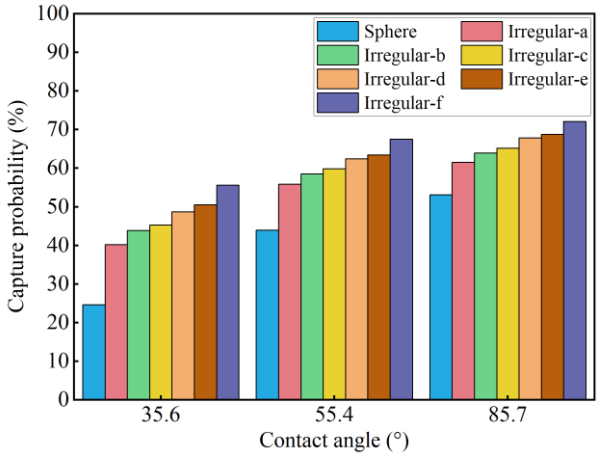

Figure 13. Effect of particle shape on the probability of bubble capturing particle.

As shown in Figure 13, at the same contact angle, the probability of a spherical particle being captured by a bubble is the smallest, and the capturing probability of irregular (a-f) particles by a bubble increase in turn. The probability of being captured by a bubble for both spherical and irregular (a-f) particles decreases with increasing contact angle, and the magnitude of the

reduction decreases with decreasing particle sphericity. For instance, the particle contact angle increased from 35.6° to 85.7°, and the capture probability between spherical particle and irregular (a-f) particles and bubble decreased by 28.47 %, 21.25 %, 20.26 %, 19.91 %, 19.15 %, 18.24 % and 16.51 %. When the contact angle is 35.6°, 55.4°, and 85.7°, the average arithmetic value of the probability of irregular (a-f) particles captured by the bubble is 13.47°, 17.28°, and 22.75° higher than that of spherical particles with the same contact angle. It means that the effect of particle shape on the probability of particles being captured by a bubble is enhanced with the weakening of particle hydrophobicity. At the same contact angle, the probability of bubbles capturing irregular shape particles increases as the sphericity of the irregular particles decreases. For example, the sphericity of irregular (a-f) particles decreases from 0.856 to 0.746, while its capture probability increases from 55.83 % to 67.50 %.

3.4 Effect of particle shape on critical induction time

The induction time generally defaults to a constant for a given particle and bubble. However, the research by Verrelli et al. [4] showed that the induction time (τ) depends on the approach trajectory of the particles, which is related to the collision angle and approach velocity of the particles can be expressed as：

$$\tau = \left[\left(\frac{73.8}{v_0}\right)^2 + \left(\frac{\varphi}{3.11°}\right)^2\right] (0.0792\, f + (1 - f)) \tag{18}$$

where:

v_0 approach velocity, mm/s

φ collision angle, °

f indicator variable, either 1 for Irregular or 0 for sphere.

For a given particle, its approach velocity is constant, so when the collision angle is the critical collision angle, the induction time is the critical induction time (maximum induction time).

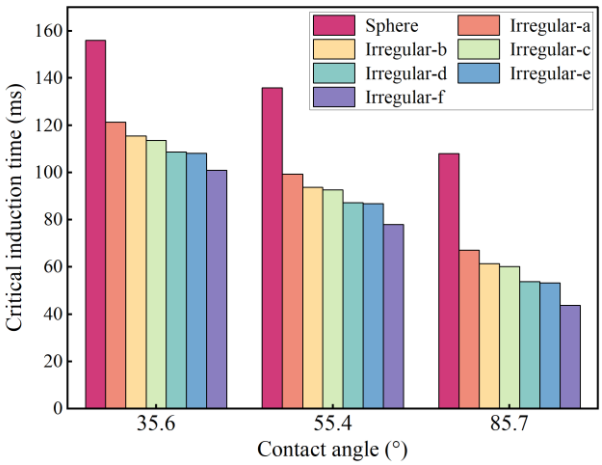

Figure 14. Effect of particle shape on critical induction time of particle.

As shown in Figure 14, at the same contact angle, the critical induction time of spherical particles is the largest, and the critical induction time of irregular shape (a-f) particles decreases with the decrease of particle sphericity. For example, when the contact angle is 55.4 °, the critical induction time of spherical particles is 136ms, the sphericity of irregular shape (a-f) particles is reduced from 0.856 to 0.746, and its critical induction time is reduced from 99.33 ms to 78 ms. At the contact angles of 35.6°, 55.4°, 85.7°, the arithmetic mean of the critical induction time of the irregular-shaped (a-f) particles was 44.60 ms, 46.33 ms, 54.44 ms lower than that of the spherical

particles of the same contact angle. It is indicated that the effect of particle shape on the critical induction time increases as the hydrophobicity of the particles decreases.

All these prove that the critical induction time of irregular particles is smaller than that of spherical particles. In other words, irregular particles' sharp and edge shapes can promote the thinning and rupturing of the liquid film between particles and bubbles during the particle-bubble interaction, thereby shortening the induction time.

To sum up, in the process of particle-bubble interaction, owing to the surface of irregular shape particles having sharp edge shapes, it is easier for irregular shape particles to rupture the liquid film between particle and bubble than spherical particles, which have the advantage of shortening the attachment time and improving the attachment probability and then improving the capture probability of bubble to irregular shape particle.

4. Conclusions

In this work, six irregular particle models with different shapes are designed. The interaction behavior of spherical particles and irregularly shaped (a-f) particles and a bubble was simulated by DEM. The effect of particle shape on particle-bubble interaction behavior, critical collision angle, capture probability, and critical induction time was investigated. The principal findings of the study are summarized below:

1. Spherical and irregularly shaped particles can be divided into five stages during their interaction with the bubble: (1) Free settling (2) Flow around the bubble surface (3) Sliding with a liquid film (4) Film rupture and TPCL formation (5) Sliding with a TPCL. However, compared with spherical particles, in film rupture and TPCL formation stage, the edges and corners of irregular particles first contact with a bubble to form TPCL, resulting in particle imbalance and rotation.
2. Irregular shape particles have the advantage of a larger critical collision angle and capture probability than spherical particles. This advantage increases with decreasing particle sphericity and enhances with decreasing particle hydrophobicity.
3. Irregular particles have a smaller critical induction time than spherical particles. Irregular particles with edges and corners can promote the thinning and rupture of the liquid film between bubble and particle.

5. References

1. Y. Xing et al., Recent experimental advances for understanding bubble-particle attachment in flotation, *Adv. Colloid Interfac.* 246 (2017)105-132, https://doi.org/10.1016/j.cis.2017.05.019
2. Y. Xing et al., Effect of surface roughness on the detachment between bubble and glass beads with different contact angles, *Powder Technoogy,* 361(2020) 812-816, https://doi.org/10.1016/j.powtec.2019.11.040
3. W. Xia, Role of particle shape in the floatability of mineral particle: An overview of recent advances, *Powder Technol.* 317 (2017) 104-116, https://doi.org/10.1016/j.powtec.2017.04.050
4. D.I. Verrelli et al., Particle shape effects in flotation. Part 1: Microscale experimental observations, *Miner. Eng.* 58 (2014) 80-89, https://doi.org/10.1016/j.mineng.2014.01.004
5. D.I. Verrelli, P.T.L. Koh and A.V. Nguyen, Particle–bubble interaction and attachment in flotation, C*hemical Engineering Science 2366* (2011) 5910-5921, https://doi.org/10.1016/j.ces.2011.08.016

6. B. Vaziri Hassas et al., Effect of roughness and shape factor on flotation characteristics of glass beads, *Colloids and Surfaces,* A. 492 (2016) 88-99, https://doi.org/10.1016/j.colsurfa.2015.12.025
7. B. Wen and W. Xia, Effect of particle shape on coal flotation, *Energy Sources, Part A.* 1339 (2017) 1390-1394, https://doi.org/10.1080/15567036.2017.1332697
8. U. Ulusoy, M. Yekeler and C. Hiçyılmaz, Determination of the shape, morphological and wettability properties of quartz and their correlations, *Minerals Engineering,* 1016 (2003) 951-964, https://doi.org/10.1016/j.mineng.2003.07.002
9. U. Ulusoy, C. Hiçyılmaz and M. Yekeler, Role of shape properties of calcite and barite particles on apparent hydrophobicity, *Chemical Engineering and Processing,* 843 (2004) 1047-1053, https://doi.org/10.1016/j.cep.2003.10.003
10. P.T.L. Koh et al., The effect of particle shape and hydrophobicity in flotation, *International Journal of Mineral Processing,* 293 (2009) 128-134, https://doi.org/10.1016/j.minpo.2009.07.007
11. M. Oja and R. Tuunila, The influence of comminution method to particle shape, *Developments in Mineral Processing,* vol. 13 (2000) C4-C64, https://doi.org/10.1016/S0167-4528(00)80028-9
12. F. Karakaş and B. Vaziri Hassas, Effect of Surface Roughness on Interaction of Particles in Flotation, *Physicochemical Problems of Mineral Processing,* vol. 52 (2016) 19-35, https://doi.org/10.5277/ppmp160102
13. R. Maxwell et al., Computer simulations of particle-bubble interactions and particle sliding using Discrete Element Method, *Journal of Colloid and Interface Science,* Vol. 381 (2012) 1-10, https://doi.org/10.1016/j.jcis.2012.05.021
14. R. Moreno-Atanasio, Influence of the hydrophobic force model on the capture of particles by bubbles: A computational study using Discrete Element Method, *Advanced Powder Technology,* vol. 424 (2013) 786-795, https://doi.org/10.1016/j.apt.2013.05.001
15. Y. Gao et al., DEM simulation of single bubble flotation: Implications for the hydrophobic force in particle–bubble interactions, *Advanced Powder Technology, vol.* 425 (2014) 1177-1184, https://doi.org/10.1016/j.apt.2014.05.020
16. Y. Gao et al., Modelling the Motion of a Collected Particle over a Bubble Surface, *Procedia Engineering,* vol. 102 (2015) 1346-1355, https://doi.org/10.1016/j.proeng.2015.01.266
17. H.J. Schulze, *Physico-chemical Elementary Processes in Flotation,* Elsevier, Amsterdam, New York, 1984.
18. P.A. Cundall and O.D.L. Strack, A discrete numerical model for granular assemblies, *Géotechnique.* 129 (1979) 47-65, https://doi.org/10.1680/geot.1979.29.1.47
19. O.I. Vinogradova and T. Fan, Hydrodynamic resistance of close-approached slip surfaces with a nanoasperity or an entrapped nanobubble, *Physical Review E,* vol. 672 (2005) 66306, https://doi.org/10.1103/PhysRevE.72.066306
20. A.V. Nguyen and H.J. Schulze, *Colloidal Science of Flotation,* Marcel Dekker, New York, 2004.
21. R. Yoon and L. Mao, Application of Extended DLVO Theory, IV: Derivation of Flotation Rate Equation from First Principles, *Journal of Colloid and Interface Science,* Vol. 181 (1996) 613-626, https://doi.org/10.1006/jcis.1996.0419
22. R.H. Yoon, The role of hydrodynamic and surface forces in bubble–particle interaction, *International Journal of Mineral Processing,* Vol. 58 (2000) 129-143, https://doi.org/10.1016/S0301-7516(99)00071-X
23. Y. Xing, X. Gui and Y. Cao, The hydrophobic force for bubble-particle attachment in flotation-a brief review, *Physical Chemistry Chemical Physics,* vol. *19* (2017) 24421-24435, https://doi.org/10.1039/C7CP03856A
24. R. Yoon, D.H. Flinn and Y.I. Rabinovich, Hydrophobic Interactions between Dissimilar Surfaces, *Journal of Colloid and Interface Science,* Vol. 185 (1997) 363-370, https://doi.org/10.1006/jcis.1996.0419

25. Z. Zhang, L. Zhao and L. Zhuang, Direct force measurement of critical detachment force between a particle and an air bubble using dynamic interaction force apparatus, *Minerals Engineering,* Vol. 159 (2020) 106627, https://doi.org/10.1016/j.mineng.2020.106627
26. Y. Gao et al., Interaction of a spherical particle with a neutrally buoyant immiscible droplet in salt solution, *Chemical Engineering Science*, Vol. 172 (2017) 182-198, https://doi.org/10.1016/j.ces.2017.07.013
27. P.A. Cundall and O.D.L. Strack, A discrete numerical model for granular assemblies, *Geotechnique.* 129 (1979) 47-65, https://doi.org/10.1680/geot.1979.29.1.47
28. Y. Tsuji, T. Kawaguchi and T. Tanaka, Discrete particle simulation of two-dimensional fluidized bed, *Powder Technology,* Vol. 177 (1993) 79-87, https://doi.org/10.1016/0032-5910(93)85010-7
29. A.V. Nguyen and G.M. Evans, Movement of fine particles on an air bubble surface studied using high-speed video microscopy, *Journal of Colloid and Interface Science,* Vol. 273 (2004) 271-277, https://doi.org/10.1016/j.jcis.2003.12.066
30. Q. Zhuo et al., Experimental Investigation of the Attachment Performance between Coal Particle and Bubble, *ACS Omega,* Vol. 6 - N. 12 (2021) 7979-7987, https://doi.org/10.1021/acsomega.0c04093
31. L. Chen, J. Wu and Z. Sun, Effect of cationic collector on the attachment of glass beads to astationary bubble, *Colloids and Surfaces A Physicochemical and Engineering Aspects,* Vol. 625 (2021), https://doi.org/10.1016/j.colsurfa.2021.126979
32. Q. Zhuo et al., The effect of collision angle on the collision and adhesion behavior of coal particles and bubbles, *Processes,* Vol. 6 (2018) 218, https://doi.org/10.3390/pr6110218
33. S. Li, et al., A CFD study of particle-bubble collision efficiency in froth flotation, *Minerals Engineering,* Vol. 141 (2019), http://doi.org/10.1016/j.mineng.2019.105855